

Experimental and Computational Investigation of a 5-inch Diameter Ducted Fan VTOL UAV in Hover and Forward Flight

Ali Akturk¹ and Cengiz Camci²

Turbomachinery and Aero-heat Transfer Laboratory, Aerospace Engineering Department,

Pennsylvania State University, University Park, PA, 16802

Ducted fan vertical take-off and landing (VTOL) uninhabited aerial vehicles (UAV) are popular because of their capacity of offering a higher static thrust/power ratio for a given diameter than open propellers. They are also known as camera/antenna carrying or sensor positioning devices. Because of their complicated missions, they need to be capable of flight in a broad range of atmospheric conditions. In forward flight, the performance of these vehicles is poor because of the distorted inlet flow. The present experimental study uses a planar particle image velocimeter (PIV) system to investigate the near duct aerodynamic performance in hover and forward flight condition. High resolution PIV measurements provide reliable aerodynamic measurements forming a validation basis for further analytical and computational design studies. A radial equilibrium based fan aerodynamic model in combination with angular momentum conservation principle and energy equation is effectively integrated into a three-dimensional RANS based computational system. PIV measurements and computational predictions of mean flow near the fan inlet plane are in very good agreement at hover conditions. The aerodynamic modifications due to fan inlet flow distortions in forward flight regime are clearly displayed in PIV results.

¹ Post-doctoral Research Fellow, Aerospace Engineering Department

² Professor of Aerospace Engineering Department

Nomenclature

β_1, β_2	= Blade inlet, exit angle measured from axial direction
c_1, c_2	= Rotor inlet, exit absolute velocity
c_θ	= Tangential (swirl) velocity component
c_x	= Axial velocity
p	= Static Pressure
P_0	= Total Pressure
ρ	= Density
r	= Radial distance measured from origin
Ω	= Rotational Speed (radian/sec)
w_1, w_2	= Rotor inlet, exit relative velocity

I. Introduction

Ducted fans that are popular choices in vertical take-off and landing (VTOL) uninhabited aerial vehicles (UAV) offer a higher static thrust/power ratio for a given diameter than open propellers. That is the result of diffusion of the propeller jet stream. They also provide an impact protection for the blades and improve personnel safety due to its enclosed fan structure as well as the lower noise level in the plane of the fan blade rotating.

The viscous flow characteristics of the ducted fan are very complex. These vehicles need to be capable of flight in a broad range of atmospheric conditions, including the complex turbulent flow fields around buildings and trees. When a VTOL ducted fan is in forward flight, because of the relative inlet flow dominantly parallel to its inlet plane, problems related to flow separation at the leading edge duct lip are encountered. The inlet flow separation leads to problems within the duct and may well result in a high pitch-up moment as the forward speed is increased. Therefore measuring and predicting the mean flow characteristics of ducted fans is crucial to understand the problems related to reliable and controllable forward flights. Numerous studies have been undertaken in order to quantify the flow field properties around ducted fans. The operation of an axial flow fan with strong inlet flow distortion severely affects the performance of the rotor

especially near the tip region of the blades.

Experimental investigation has been the major approach to study the mean flow characteristics of the ducted fan. Abrego and Bulaga [1] performed wind tunnel tests to determine the performance characteristics of ducted fans for axial and forward flight conditions. Their study resulted in showing important effect of exit vane flap deflection and flap chord length on providing side force. Martin and Tung [2] tested a ducted fan VTOL UAV with a 10-inch diameter fan rotor. They measured aerodynamic loads on the vehicle for different angle of attacks in hover and different crosswind velocities. They also included hot-wire velocity surveys at inner and outer surface of the duct and across the downstream wake emphasizing the effect of tip gap on the thrust force produced. In addition, their study showed the effect of leading edge radius of the duct on the stall performance and stability of the vehicle. Fleming, Jones and Lusardi [3] et. al. conducted wind tunnel experiments and computational studies around a 12-inch diameter ducted fan. They concentrated on the performance of ducted fan VTOL vehicles in crosswind.

Moreover, the ducted fan design and performance analysis were widely performed by using computational flow modeling. Lind, Nathman and Gilchrist [4] carried out a computational study using a panel method. They compared their results to the experimental results from Martin and Tung [2]. Graf, Fleming and Wings [4] improved ducted fan forward flight performance with a recently designed leading edge geometry which was a significant factor in offsetting the effects of the adverse aerodynamic characteristics. He and Xin [5] developed the ducted fan models based on a non-uniform and unsteady ring vortex formulation for duct and blade element model for fan. Numerical study in both flight conditions, axial flight and cross wind ~~condition flight~~ were conducted and validated with measured data. Chang and Rajagopalan [6] developed an accurate grid generation methodology known as “the curve adaptive option” to model several industrial ducted fans. An axisymmetric, incompressible Navier-Stokes solver was applied to calculate the flow field of a duct fan. The computational results agreed well with available wind tunnel test data. Ahn and Lee [7] applied a computational method to their ducted fan system to identify the design parameters which affect its performance. Their ducted fan system was designed by using the stream-surface based axisymmetric analysis which provided the physical characteristics and design

parameters of the system. Lind, Ko, Ohanian and Gelhausen [8] developed a computer code aiming the preliminary design of a ducted fan system. This code was validated using data from many wind tunnel and flight tests. Further, it was extensively used in the design of commercial ducted fans. Recently, Zhao and Bil [9] proposed a CFD simulation to design and analyze an aerodynamic model of a ducted fan UAV in preliminary design phase with different speeds and angles of attack.

The current study uses experimental and computational analysis around a ducted fan that has a 5-inch diameter. By these analyses, complicated flow field around the ducted fan in hover and forward flight conditions is investigated. Flow features such as inlet lip separation, distortion of inlet flow features before and after the axial fan rotor, influence of rotor tip speed, influence of forward flight velocity and the interaction of the cross wind with fan exit jet are investigated through experiments and computations. For high-resolution mean flow experiments, a particle image velocimeter (PIV) is used. Axial and radial velocity components at the inlet/exit region of the ducted fan are measured in hover and forward flight. By measuring axial and radial velocity components, the effect of leading edge duct lip separation on the flow field into the fan rotor is analyzed.

For the computational investigations, three-dimensional incompressible Reynolds Averaged Navier-Stokes (RANS) equations are solved using a commercial solver, FLUENT. In order to accelerate the viscous flow computations, a rotor disk model based on radial equilibrium equation, energy equation and the conservation of angular momentum principle is integrated into the viscous flow solver. The specific ~~actuator disk~~ based fan-model uses a prescribed static pressure rise across the rotor disk for a time efficient simulation of the fan rotor. The paper describes a method to compute the static pressure rise at each radial position of the rotor blade in function of the rotor exit absolute velocity.

Please not that there is a section/insert here

II. Experimental Setup

A test rig is designed and manufactured to investigate the local flow features in and around a 5" diameter ducted fan using a planar PIV system. The set-up has also provisions for seeding

the fan flow field with a smoke generator based on a fluidized based system using fog fluid which is a mixture of triethylene glycol, propylene glycol, butylene glycol and de-ionized water. Figure 1 shows a sketch of the experimental setup.

A. Ducted Fan Model

The five bladed ducted fan rotor is driven by a brushless DC electric motor. This motor is speed controlled by an electronic speed control (ESC) system. The high efficiency electric motor driving the fan can deliver 1.5 kW power (2.14 HP) and spin 1050 rpm per volt supplied to the motor. The phase-locked PIV measurements are triggered by using an optical once-per-revolution device located near the hub of the rotor exit. An infrared beam is reflected from a highly reflective surface (1 mm wide shiny metallic film) attached to the rotor hub. This once-per-rev pulse provides a phase-locked triggering of the PIV data collection system. The position of the rotor can be adjusted accurately in relation to the position of the laser light sheet that contains the rectangular PIV measurement domain. The PIV domain can be located at the upstream and downstream of the rotor as shown in Figure 1. Figure 2 shows the five bladed ducted fan that is used in the present PIV experiments. The geometric specifications are presented in Table 1.

This ducted fan unit is designed for small scale uninhabited aircraft. This unit is manufactured from carbon composite material and has six vanes at the exit of the fan in order to remove some of the swirl and torque existing at the exit of the rotor. A tail cone is used to cover the motor surface and hide the electrical wiring.

B. Crosswind Blower

Figure 1 shows a sketch of the crosswind blower that can generate about 6 m/s uniform mean flow just upstream of the ducted fan unit. The axial flow fan driving the cross wind blower is capable of generating $5.58 \text{ m}^3/\text{s}$ (10,594 cfm). There is a wire mesh screen at just downstream of the axial flow fan. The flow passes through a 10 inch wide flow straightener section. Finally, there is a perforated plate (50% open area) at the exit of the crosswind blower. The grill, flow straightener

Rotor hub diameter	52 mm
Rotor tip diameter	120 mm
Blade height h	34 mm
Tip clearance t/h	5.8 %
Max blade thickness at rotor tip	1.5 mm
Tailcone diameter	52 mm
Tailcone length	105 mm
Rotor blade section properties	
	Hub Mid Span Tip
Blade inlet angle β_1	60° 40° 30°
Blade exit angle β_2	30° 45° 60°
Blade chord	32 mm 30 mm 28 mm

Table 1 Geometric specifications of five inch ducted fan

and the perforated plate at the exit provide a uniform mean flow at the exit of the system. The uniformity of the blower exit mean flow (6 m/s) is determined by a hot wire anemometer. The measured turbulence intensity of the uniform flow is less than 1 % based on the rms fluctuation velocity fluctuations normalized by the mean flow magnitude. An AC inverter connected to the three phase AC motor of the axial fan unit can adjust the rotor rpm and mean flow velocity magnitude.

ALi is there a J ratio we can give here (a typical value)

III. Experimental Method

A. Planar Particle Image Velocimety (PIV)

Measurement Technique

The PIV technique [10–14] measures instantaneous velocity components of a flow field over a determined area. Small particles existing in a fog generated by a fluidized bed system are introduced into the fluid flow, and the region of interest is illuminated by a light sheet provided by short Nd-Yag laser pulses lasting as short as a few nanoseconds. The subsequent step is the recording of the displacement of particles via one or two CCD cameras depending on the specific

PIV technique used. ~~A comprehensive explanation of this technique is given by R.J. Adrian [10, 13].~~
~~As a summary, four basic steps should be mentioned in an experimental procedure;~~

- Flow is seeded.
- The flow region of interest is illuminated.
- Scattering light from the particles forming the speckle images is recorded by cameras.
- Recordings are analyzed by means of a correlation based software system.

In this current study, the inlet and exit mean flow performance of a 5-inch diameter ducted fan was quantified by using the PIV technique. Axial and radial components of velocity profiles were measured near the inlet and exit planes of the ducted fan. Two separate measurement domains of [156 mm x 96 mm] are used in inlet and exit flow. Figure 1 illustrates the PIV setup in which the fan exit field is measured by keeping the PIV light sheet unchanged. For the measurement of inlet flow velocities, the ducted fan is flipped vertically. The PIV measurement domains are illuminated by a double cavity frequency doubled pulsating Nd-Yag laser which has an emitted radiation wavelength of 532 nm (green) and 120 mJ pulse energy level. Pairs of images from measurement domains are captured by an 80C60 HiSense PIV/PLIF camera. A CCD camera is positioned normal to the laser sheet.

In planar PIV measurements, two components of the velocity vector are measured in the plane illuminated by a laser sheet. The current study focuses on measuring the axial and radial components of the local velocity vectors. These measurements are based on the image maps obtained by the CCD camera. The size of seeding particle is 0.25-60 μm . The image pairs of PIV domains are recorded. The image maps are divided into 32 x 32 pixel interrogation areas and 25% overlapping is used. “*Flowmap*” software provided by DANTEC [14] used for capturing PIV images and correlation analysis. All 700 image pairs are adaptive correlated, moving average validated and then ensemble averaged to obtain true mean flow. The ensemble size is of critical importance in achieving statistically stable mean velocity distributions in any PIV data reduction process. Figure 3 presents the influence of ensemble averaging sample size on the spanwise distribution of the

most significant velocity component that is axial component. Figure 3 indicates that an ensemble size of 400 is sufficient in achieving a statistically stable average in the current set of experiments.

IV. Computational Method

A. Radial Equilibrium Based Analysis of Ducted Fan in Hover and Forward Flight

A simulation of the mean flow field around the ducted fan was performed by using a commercial code Ansys-Fluent [15]. The specific computational system solves the 3D Reynolds-Averaged Navier-Stokes equations using a finite volume method. The transport equations describing the flow field are solved in the domain that is discretized by using an unstructured computational mesh. For the analysis of the flow field around ducted fan rotors, there are many computational modeling options in general purpose fluid dynamics solvers. The most complex and time consuming computational model is the modeling of unsteady/viscous/turbulent flow in and around the fan rotor by using an exact 3D model of rotor geometry using a sliding mesh technique. This type of solution is usually lengthy and requires significant computer resources especially in the forward flight mode when an axisymmetric flow assumption is not applicable. The current RANS computations use a simplified rotor model termed as “*Actuator disk model*” for the generation of the general inviscid flow features of the fan rotor. A $k-\epsilon$ turbulence model was invoked for the current computations, in areas other than the actuator disk. Figure 4 shows a flowchart of the method used.

B. Boundary Conditions

1. Hover

Figure 5 shows the specific boundary conditions and computational domain size implemented in the solver for hover condition. The duct and tailcone surfaces are considered as solid walls with no-slip condition. On the side surfaces, a symmetry condition is assumed. For the hover condition, a pressure inlet boundary is assumed on the top surface. Atmospheric static pressure is prescribed on the top surface. Pressure inlet boundary is treated as loss-free transition from stagnation to inlet conditions. The solver calculates the static pressure and velocity at the inlet. Mass flux

through boundary varies depending on interior solution and specified flow direction. Pressure outlet boundary condition is assumed on the bottom surface for hovering condition. Pressure outlet boundary interpreted as atmospheric static pressure of environment into which the flow exhausts. ~~An additional “Fan” type condition was used for the implementation of the specific actuator disk model described in section IV C.~~

2. Forward Flight

Figure 6 shows the specific boundary conditions implemented in the solver for forward flight. Like hover condition, the duct and tailcone surfaces are considered as solid walls with no-slip condition. Velocity inlet boundary condition is assigned on the windward side of the computational domain. Using this boundary condition velocity and turbulent intensity at the windward side is prescribed. For the leeward side of the domain an outflow condition is assigned. For the top, bottom and remaining side surfaces symmetry boundary condition is assigned. Like the hover condition, “Fan” type condition was set using an “*actuator disc model*” replacing the ducted fan rotor. Details of the actuator disk model is explained in section IV C.

C. Actuator Disk Model

The complex 3D rotor flow field in the rotating frame of reference is replaced by a simplified “*actuator disc model*” originating from the simultaneous use of the radial equilibrium equation, energy equation and the conservation of angular momentum principle across the fan rotor. The radial equilibrium equation is the force balance in the radial direction at a given axial position, balancing the pressure forces in radial direction with the centrifugal force. The viscous effects are ignored in this simplified and easy to implement “*actuator disc model*”.

In this approach, a pressure change term is computed at each radial position of the rotor from hub to tip. The magnitude of the static pressure jump term across the rotor is closely related to the amount of stagnation enthalpy change from the rotor inlet to exit. The stagnation enthalpy increase from the rotor inlet to exit is the same as the rate of energy provided to the fluid by the

rotor per unit mass flow rate of the duct flow. The conservation of angular momentum principle and energy equation suggests that the magnitude of this jump is mainly controlled by the tangential (swirl) component $c_{\theta 2}$ of the flow velocity in the absolute frame of reference at the exit of the rotor and rotor angular velocity.

Figure 7 presents the velocity triangles of the ducted fan rotor at inlet (1) and exit (2). β_1 and β_2 are the blade inlet and exit angles measured from the axial direction. Since the tip Mach number (0.28) of the rotor is not in the compressible flow range, it is reasonable to assume that the internal energy at the rotor inlet e_1 and exit e_2 is the same, $e_1=e_2$. In a ducted fan rotor, it is realistic to assume that the “axial component” of the absolute velocity vector is also conserved from inlet to exit $c_{x2}=c_{x1}$. The flow is assumed to be axial at rotor inlet where $c_1=c_{x1}$ and $c_{\theta 1} = 0$ under design conditions. The relative velocity vector at the exit of the rotor w_2 is smaller than the relative velocity w_1 at the rotor inlet. While the relative flow w_2 is diffusing in the relative frame of reference, the absolute flow velocity vector c_2 is accelerated at the rotor exit, because of added energy to the flow by the rotor.

Equation 1 represents the change of stagnation enthalpy in the ducted fan rotor system. The right hand side of this equation is the rate of work per unit mass flow rate of air passing from the rotor. The right hand side is also the same as the product of the rotor torque and angular speed of the fan rotor.

$$h_{O2} - h_{O1} = U(c_{\theta 2} - c_{\theta 1}) \text{ where } U = \Omega r \text{ and } c_{\theta 1} = 0 \quad (1)$$

$$(h_2 + c_2^2/2) - (h_1 + c_1^2/2) = U c_{\theta 2} \quad (2)$$

$$\left(e_2 + \frac{p_2}{\rho_2} + c_2^2/2 \right) - \left(e_1 + \frac{p_1}{\rho_1} + c_1^2/2 \right) = U c_{\theta 2} \quad (3)$$

Equation 1 is a simplified form of the energy equation from rotor inlet to exit of a ducted fan unit. When $e_1=e_2$ is substituted into equation 3 because of incompressibility condition, the “Euler equation” or “pump equation” results in as equation 4. Using equations 4 and 5, an equation for the calculation of static pressure jump between the rotor inlet and exit can be obtained.

The determination of $c_{\theta 2}$ is performed by using the velocity triangles in Figure 7. Since the blade inlet/exit angle distribution for 1 and 2 in radial direction is known from the existing rotor geometrical properties, shown in Table 1. w_2 can be calculated from the assumption that $c_{x2}=c_{x1}=c_1$. The absolute rotor exit velocity c_2 is determined by adding $U = \Omega r$ to w_2 in a vectorial sense.

Equation 4 could be rearranged as follows.

$$\frac{1}{\rho} (P_{O2} - P_{O1}) = U c_{\theta 2} \quad (4)$$

By expressing (p2-p1) a pressure jump in function of radius could be obtained.

$$\left(p_2 + \rho \frac{c_2^2}{2} \right) - \left(p_1 + \rho \frac{c_1^2}{2} \right) = \rho U c_{\theta 2} \quad (5)$$

$$\Delta p = p_2 - p_1 = \rho \left[U c_{\theta 2} - \frac{1}{2} (c_2^2 - c_1^2) \right] \quad (6)$$

Equation 6 allows enforcing a prescribed pressure jump p in function of density, radial position, rotor angular speed Ω , rotor exit swirl velocity $c_{\theta 2}$, c_1 and c_2 . The rate of energy (per unit mass flow rate) added to the flow by the rotor is specified by the product $U c_{\theta 2}$ as shown in equations 4 and 5. Equation 6 could be evaluated at each radial position between the rotor hub and tip resulting in the radial distribution of the static pressure jump required by the general purpose viscous flow solver for a “*Fan*” type boundary condition. Δp can be effectively specified in a user defined function “*UDF*” in the solver. The “*Fan*” type boundary condition is an effective and time efficient method of implementing a rotor flow field via an “*actuator disk model*” in a 3D viscous flow computation.

V. Experimental Results in Hover and Forward Flight Conditions

Experiments were performed at two different rotational speeds at 9000 and 15000 rpm. The performance of the ducted fan was analyzed in hover and forward flight conditions. The forward flight condition is simulated with a crosswind of 6 m/s velocity produced by the crosswind blower shown in Figure 1.

Figures 8a and 9a show streamlines obtained from PIV measurements at different rotational

speeds (9000 and 15,000 rpm) in hovering. The figures are contour plotted and colored with the magnitude of measured velocity. As expected, the magnitude of velocity is increasing at both inlet and exit regions by increasing rotational speed of the fan rotor. The streamline structure and the local magnitude of the velocity vector show a reasonable axisymmetry in hover mode as shown in Figures 8a and 9a. The exit jet from the fan unit show a visible flow entrainment from the still air region into the exit jet at both rotational speeds. In addition to the flow entrainment, the exit jet region at 15,000 rpm exhibit slight momentum deficit near $x=0.1\text{m}$. This momentum deficit could be explained with the existence of the wakes of the six bladed exit guide vanes in the fan unit. The final form of this distribution is also controlled by the unique rotor position defined by the current phase-locking approach.

Figure 8b illustrates the change of inlet/exit flow field caused by the forward flight effect at 9000 rpm. With the influence of the crosswind at 6 m/s, the distribution of the velocity magnitude at the inlet is distorted due to the separation from the leading side duct lip. Due to the separation region, the breathing area of the fan rotor is reduced. At the leading side of the duct, maximum velocity magnitude is shifted towards to hub because of the effect of lip separation.

Figure 10 clearly supports the observation that the “*leading side*” peak in axial velocity at the inlet plane is shifted towards the rotor hub due to inlet lip separation. However, the trailing side peak in inlet plane is shifted towards the blade tip. When the peak is shifted towards the rotor tip section, the work addition to fan exit flow is more significant as shown in Figure 10. Due to more distorted inflow at the leading side, exit flow average velocity magnitude is slightly decreased at the leading side. The streamlines near the trailing side at the inlet plane are more normal to the fan inlet plane indicating slightly higher mass flow rate on this side than the leading side. The trailing side of the duct is affected less from the crosswind. Streamlines at the exit flow clearly show the influence of forward flight velocity on the high momentum jet exit fluid. With the effect of the crosswind, the exit jet is deflected and pushed towards to the tip of the tail cone surface at the leading side. The trailing side is affected less than the leading side as expected.

Axial velocity plot shown in Figure 10 is drawn along a horizontal line 3 mm away from the exit and inlet surfaces to demonstrate the effect of crosswind velocity on the axial velocity

component. Introduction of crosswind simulates the forward flight results in a reduced axial velocity near the leading edge duct lip. That can be explained by the occurrence of a separation bubble on the leading side lip inside the duct. Figure 10 also indicates that the axial velocity near the trailing side lip is relatively enhanced when compared to the hover condition.

Figure 9b shows the effects of forward velocity at 15000 rpm. An increase in the rotational speed at forward flight, effectively energizes the air flow at the inlet. The effect of separation at the leading edge is reduced by increasing rotational speed of the fan. The streamlines near the inlet are more normal to the inlet surface at 15000 rpm. The streamlines in the exit jet area are much less influenced by the mainstream flow. Figure 9a shows that the mass flow rate passing from the ducted fan at 15000 rpm is much higher than the case for 9000 rpm. The axial velocity peak in exit plane is almost doubled when the rotational speed is increased to 15000 rpm.

Figures 11 and 12 illustrates the axial and radial velocity components at 9000 and 15000 rpm for hover condition. Increase in axial velocity by a rotational speed increase, results in a significant enhancement of axial momentum of the system. The radial velocities that are usually in much smaller magnitudes than the axial components show a symmetrical distribution with respect to the axis of rotation. The axial and radial velocity components in hover condition results in a reasonably uniform distribution of side forces around the duct.

Introducing a crosswind velocity to the field changes the distribution of radial flow velocity around the duct. Figures 13b and 14b indicates an abrupt increase near the leading side of the duct lip. That increase in radial velocity is the result of the strong re-circulatory flow near the leading side as expected. The flow non-uniformities near the leading side of the lip and the strong variations between the leading and the trailing side of the exit jet result in strong pitch-up moment acting on the ducted fan. It is also observed that by the increase of rotational speed, the radial velocity is also increasing. But the same amount of increase can also be seen on the radial velocity distribution in hovering mode. As increasing rotational velocity, axial momentum of the flow is increased. The mass flow rate passing through the duct is increasing by rotational speed of fan rotor. The increased mass flow rate produces stronger fan exit flow.

VI. Computational Results

1. Grid Refinement Study

A grid independence study was performed to show that the computational results are not dependent on the computational mesh and that the resolution of the mesh is adequate to capture the significant flow characteristics. The grid independency is evaluated by comparing the computational solutions from 3 different mesh sizes, comprising a coarse mesh with 350,000 nodes, a medium mesh with 750,000 nodes and a fine mesh with 1,200,000 nodes. The axial velocity distributions at the exit of ducted fan are plotted as shown in figure 15 for three different grid densities. The profile suggests that the computational results are reasonably grid independent when the 750,000 grid node number is exceeded. Therefore, the medium mesh is used for all predictions in this chapter. Figure 16 shows a view from the mesh used in computations.

A. Model Validation at hover and forward flight

Hover Condition Results

In this section, the results of 3D computations are compared to the PIV experiments performed on the 5-inch diameter ducted fan. The computed axial velocity component at 3 mm away from the duct inlet surface is compared to the results of PIV measurements as shown in Figure 17. The computational and experimental results are in good agreement near the leading side of the fan at the inlet plane. The computational predictions near the leading side and the trailing side show an almost symmetrical axial velocity distribution.

The simulation underpredicts the flow as measured by PIV near the trailing side of the duct as shown in Figure 17. In a phase-locked PIV approach, measurements are always performed at the same circumferential position of the rotor blade. Since we used a five bladed fan rotor, the right side of the domain in Figure 17 contains a rotor blade in the laser sheet. However the left side of the domain where $r \leq 0$ does not contain a rotor blade in the laser sheet. The slight underprediction is related to the specific phase-locked position of the rotor during the PIV measurements. Because of the blockage effect introduced by the rotor blade in the laser sheet plane, the PIV measured axial

flow velocity magnitude is slightly altered when compared to the computational result.

The comparison of PIV measurements and computed axial velocity components at 3 mm away from the duct exit surface are shown in figure 18. Since the computational method doesn't have any tip loss related term, there is an over prediction of axial velocity near the casing of the ducted fan. It can also be observed that the rotating rotor hub related losses are not predicted well by computations.

Figure 19 shows comparison of contour plots obtained from computational predictions and PIV measurements. Computational results are slightly over predicting the measured axial velocity at the inlet of the ducted fan. In addition, predictions near the hub is lower than the measurements, because the rotating hub is not simulated in computations. The hub separation usually exists in small diameter low Reynolds number ducted fan rotors. The current actuator disk approach neglects the hub separation features acting in the 5-inch diameter ducted fan.

Forward Flight Condition Results

The comparison of PIV measurements and computed axial velocity components are shown in figure 20 for 6 m/s forward flight. Axial velocity computed at the inlet of the ducted fan shows good agreement with PIV measurements. Flow near the hub is underpredicted because the rotating hub effect is not included in computations. It is also noted that the exit axial velocities are overpredicted. At the windward side of the ducted fan, axial velocities are disturbed at the exit windward side of the ducted fan. Losses are shown to be higher in PIV results near the tailcone at the leeward side of the ducted fan.

VII. Summary

The velocity field around the ducted fan was measured using a planar PIV system. Axial and radial velocity components at the inlet/exit region of the ducted fan were measured in hover and forward flight at 6m/s.

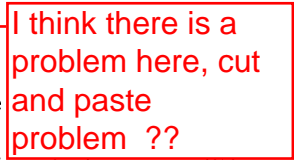
Beside the experimental study, a computational study based on solving incompressible Navier-Stokes equations was carried out. The specific actuator disk based fan-model developed in this study uses a prescribed static pressure rise across the rotor disk for a time efficient simulation

of the fan rotor.

The results of the PIV measurements have proven that the performance of the ducted fan was highly affected from the crosswind velocity. In crosswind, by the effect of the forward flight velocity, a separation region restricting the effective breathing area of the fan rotor, was always observed at the leading side of the ducted fan. That separation bubble significantly affects the exit flow of the fan rotor.

By the introduction of inlet distortion at the leading side, the flow characteristics of the fan were highly altered compared to the fan design conditions. The inlet flow distortion due to the leading side lip separation results in a measurable drop in thrust force generated by the system.

The measured differentials existing between the leading side and trailing side of inlet flow are likely to generate excessive moment imbalance during the forward flight of the ducted fan based V/STOL UAV. The measured local flow differentials at the inlet plane directly translate into non-uniformities in the exit jet of the ducted fan.

indent The experimental results showed that an increase of the fan enhances the axial velocity component at the inlet and exit sections in hover condition, as expected. That increase in the rotational speed of the fan rotor has proven to improve the performance of the ducted fan in forward flight due to improved axial momentum change in the ducted fan.

An increase in the rotational speed of the fan from 9000 rpm to 15000 reduced the effect of the leading side separation bubble.

The radial equilibrium based computational analysis was able to predict the inlet flow axial flow velocity distribution well at the 9000 rpm hover condition.

References

- [1] Abrego, A. I. and Bulaga, R. W., "Performance Study of a Ducted Fan System," *AHS Aerodynamics, Aeroacoustic , Test and Evaluation Technical Specialist Meeting*, 2002.
- [2] Martin, P. and Tung, C., "Performance and Flowfield Measurements on a 10-inch Ducted Rotor VTOL UAV," *60th Annual Forum of the American Helicopter Society*, 2004.
- [3] Fleming, J., Jones, T., Lusardi, J., Gelhausen, P., and Enns, D., "Improved Control of Ducted Fan

- VTOL UAVs in Crosswind Turbulence,” *AHS 4th Decennial Specialist’s Conference on Aeromechanics*, 2004.
- [4] Graf, W., Fleming, J., and Wing, N., “Improving Ducted Fan UAV Aerodynamics in Forward Flight,” *46th AIAA Aerospace Sciences Meeting and Exhibit*, 2008.
- [5] He, C. and Xin, H., “An Unsteady Ducted Fan Model for Rotorcraft Flight Simulation,” *62th AHS Forum*, 2006.
- [6] Chang, I. C. and Rajagopalan, R. G., “CFD Analysis for Ducted Fans with Validation,” *21th AIAA Applied Aerodynamics Conference*, 2003.
- [7] Ahn, J. and Lee, K. T., “Performance Prediction and Design of a Ducted Fan System,” *40th AIAA/ASME/SAE/ASEE Joint Propulsion Conference and Exhibit*, 2004.
- [8] Lind, R., Nathman, J. K., and Gilchrist, I., “Ducted Rotor Performance Calculations and Comparisons with Experimental Data,” *44th AIAA Aerospace Sciences Meeting and Exhibit*, 2006.
- [9] Zhao, H. W. and Bil, C., “Aerodynamic Design and Analysis of a VTOL Ducted-Fan UAV,” *26th AIAA Applied Aerodynamics Conference*, 2008.
- [10] Adrian, R., “Particle Imaging Techniques for Experimental Fluid Mechanics,” *Ann. Rev. Fluid Mech.*, Vol. 23, 1991, pp. 261–304.
- [11] Kahveci, H. S. and C. C., “Flow Around Helicopter Blade Tip Sections Using 2D Particle Image Velocimeter-Part I,” *11th Int. Symp. on Transport Phenomena and Dynamics of Rotating Machinery (ISROMAC-11)*, , No. 136, 2006.
- [12] Kahveci, H. S. and C. C., “Flow Around Helicopter Blade Tip Sections Using A (3D) Stereoscopic Particle Image Velocimeter-Part II,” *11th Int. Symp. on Transport Phenomena and Dynamics of Rotating Machinery (ISROMAC-11)*, , No. 137, 2006.
- [13] Kahveci, H. S., *Implementation of a Stereoscopic PIV in Rotating Machinery Including Helicopter Rotor Flows*, Master’s thesis, The Pennsylvania State University, University Park, PA, 2004.
- [14] DANTEC, “FlowMap Particle Image Velocimetry Instrumentation-Installation & User’s Guide,” 2000.
- [15] ANSYS, “ANSYS-FLUENT v12 User’s Guide,” 2009.

Follow the last
name first initial
format

It is best just to
name this in the
manuscript.
Software manuals/
guides are not
considered quality
archival
references.

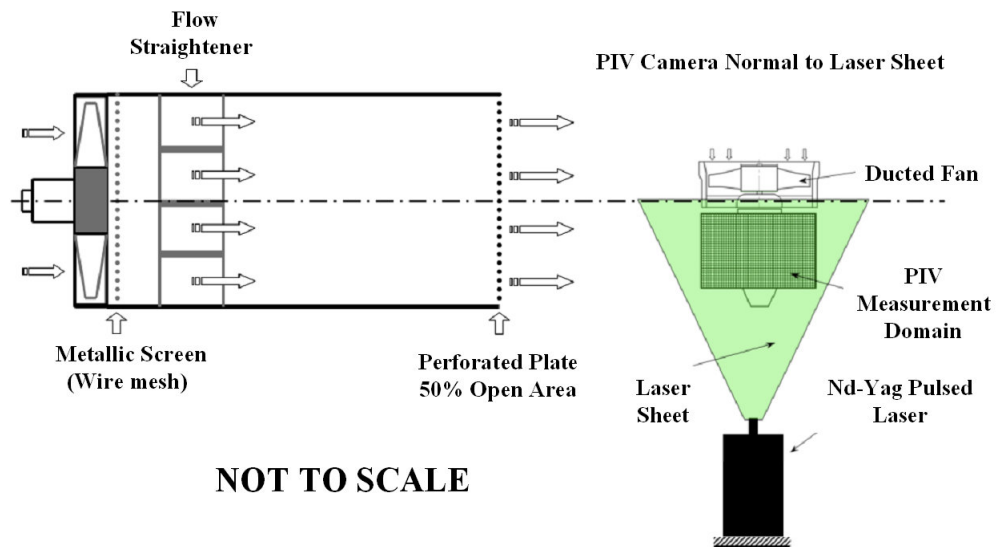


Fig. 1 Cross wind blower, the ducted fan and the PIV system orientation

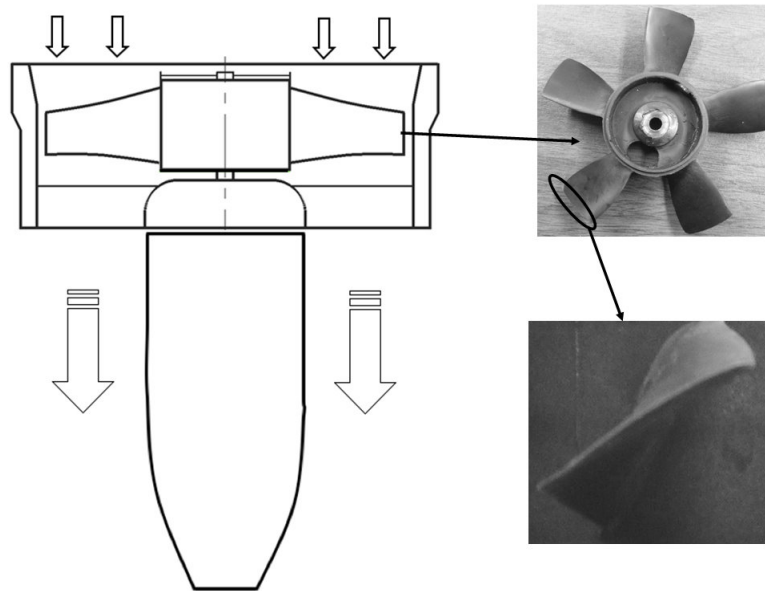


Fig. 2 Five inch diameter five-bladed ducted fan

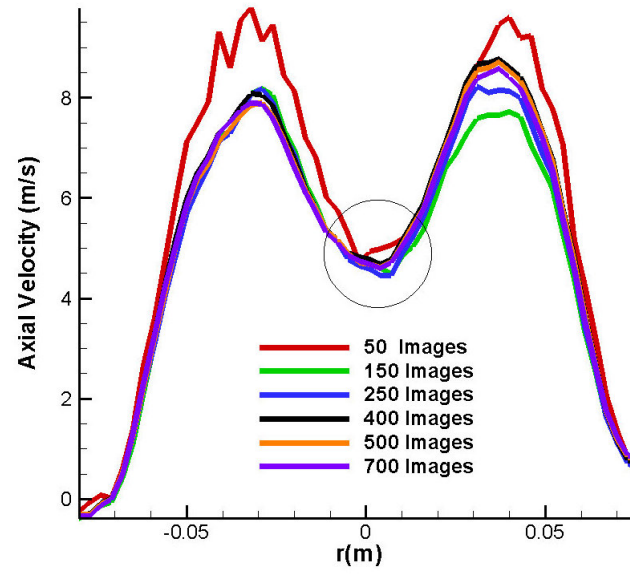


Fig. 3 Influence of ensemble averaging “*image sample size*” on the axial velocity component

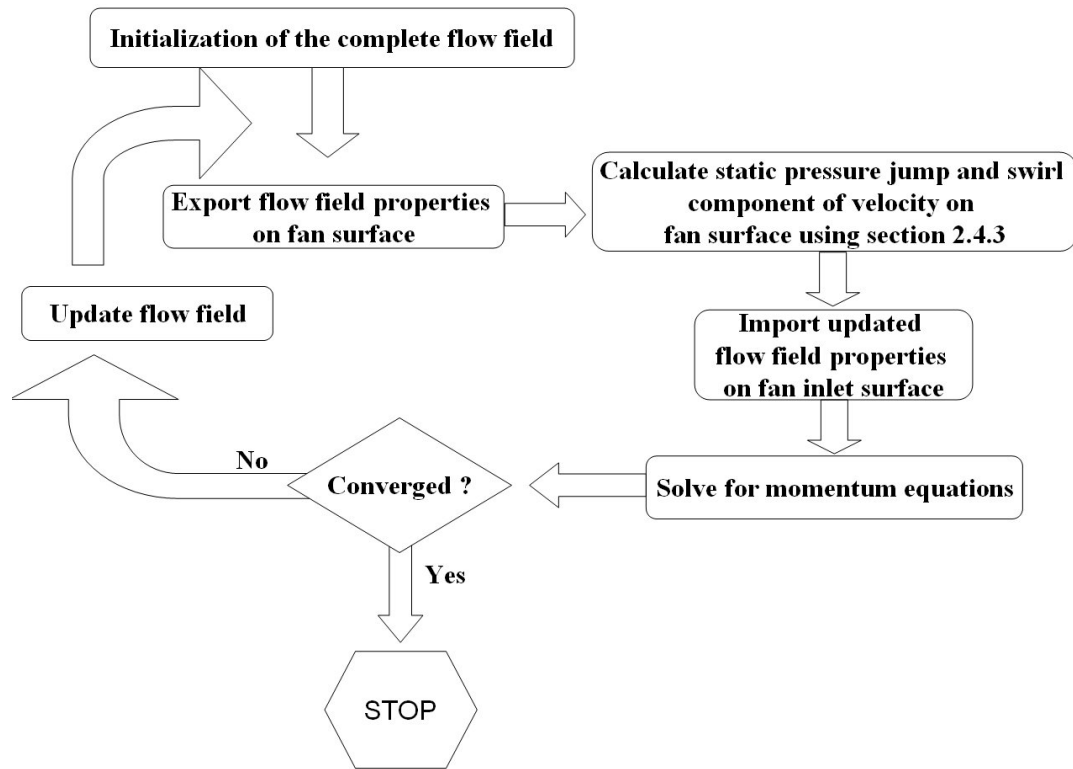


Fig. 4 Flowchart of the 3D RANS based computational method including the actuator disk.

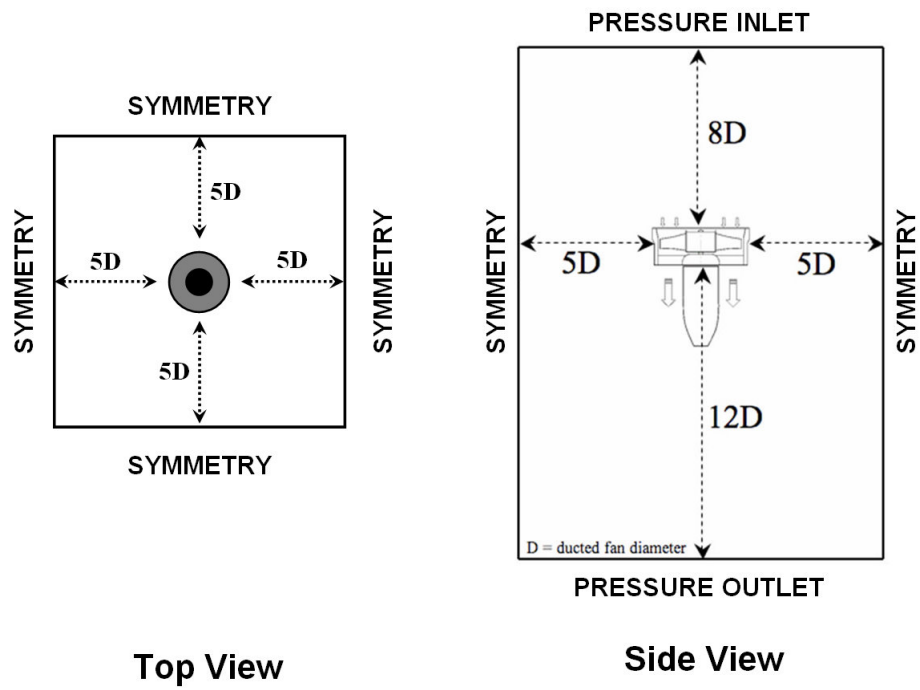


Fig. 5 Boundary conditions for hover

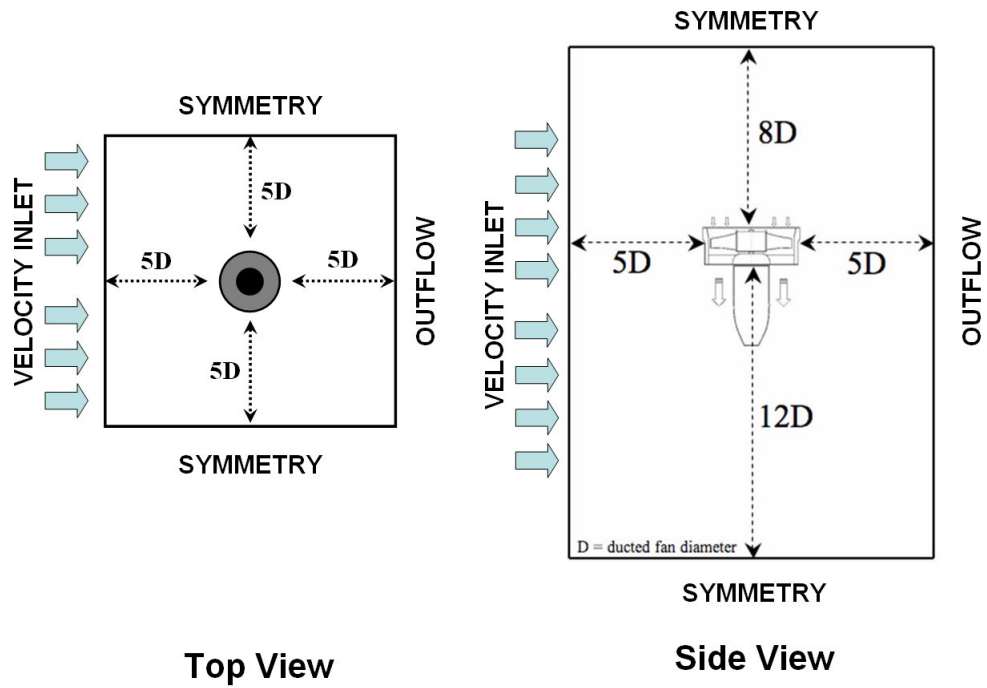


Fig. 6 Boundary conditions for forward flight

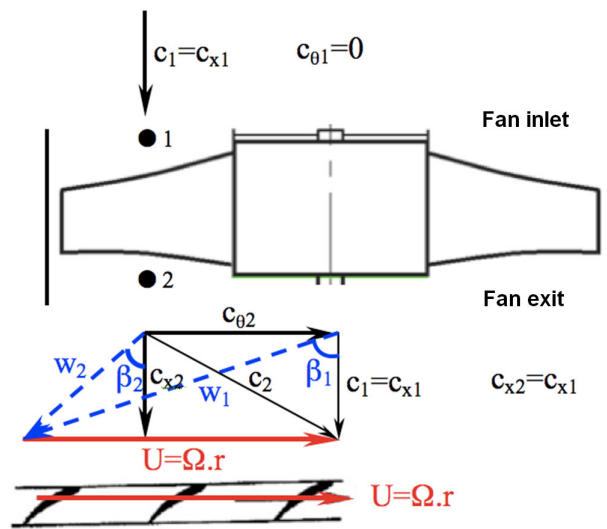


Fig. 7 Velocity triangles at the inlet and exit of the ducted fan rotor

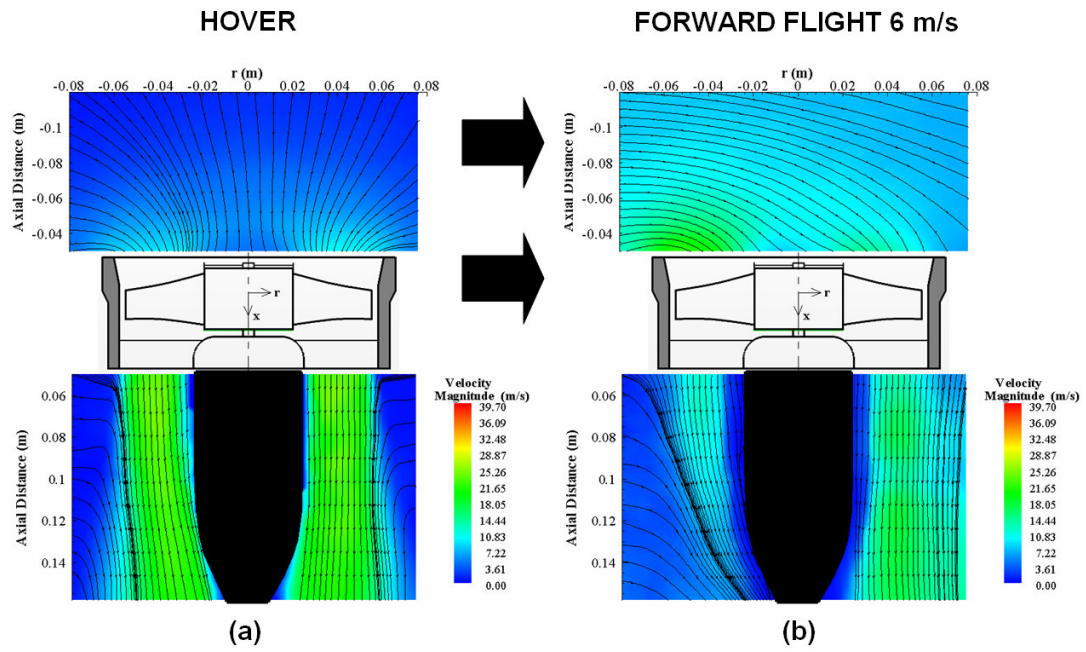


Fig. 8 Streamlines at inlet and exit of ducted fan for HOVER (a) and FORWARD FLIGHT (b) (PIV measurements at 9000 rpm)

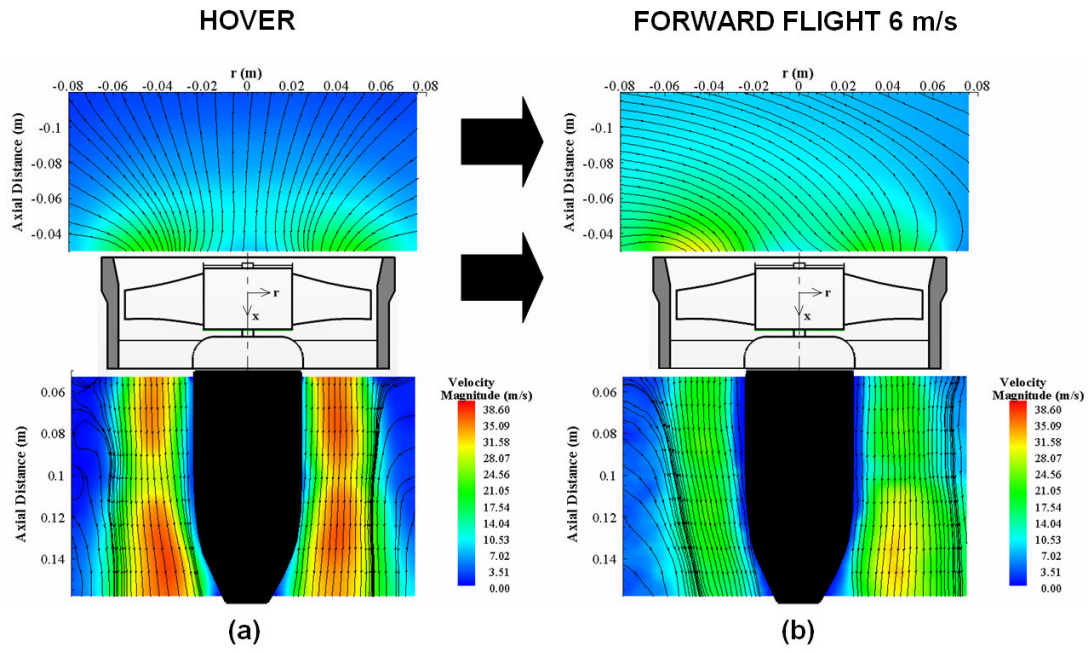


Fig. 9 Streamlines at inlet and exit of ducted fan for HOVER (a) and FORWARD FLIGHT (b) (PIV measurements at 15000 rpm)

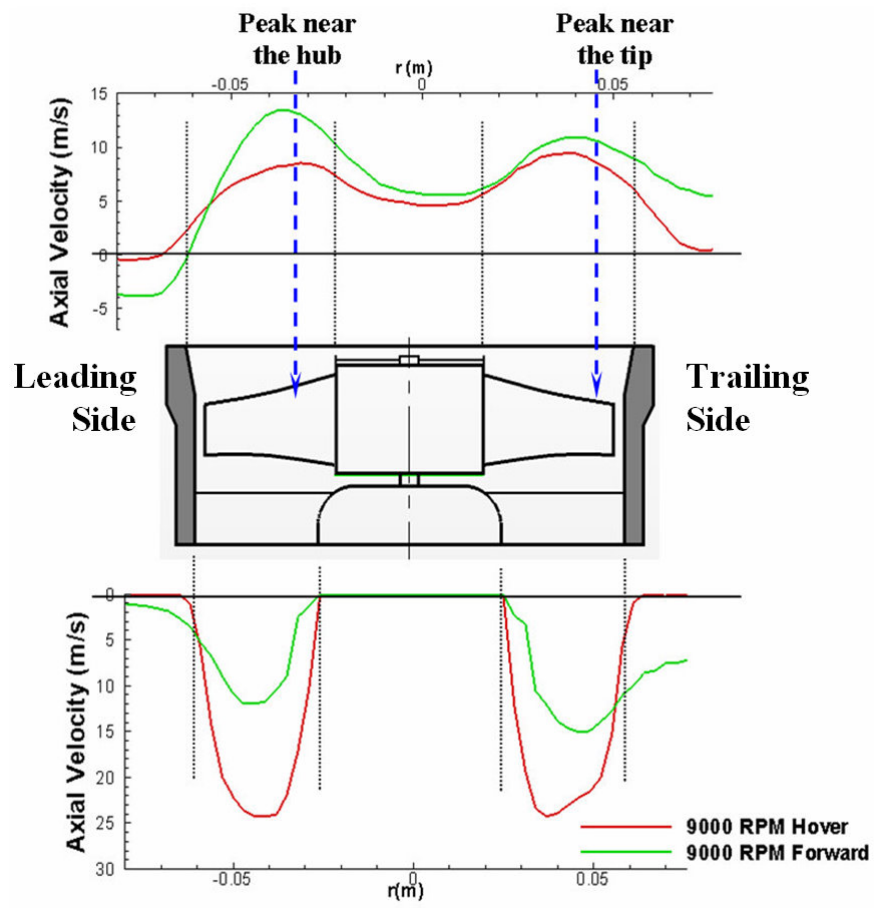


Fig. 10 Axial Velocity Distribution at the inlet and exit of ducted fan at 9000 rpm

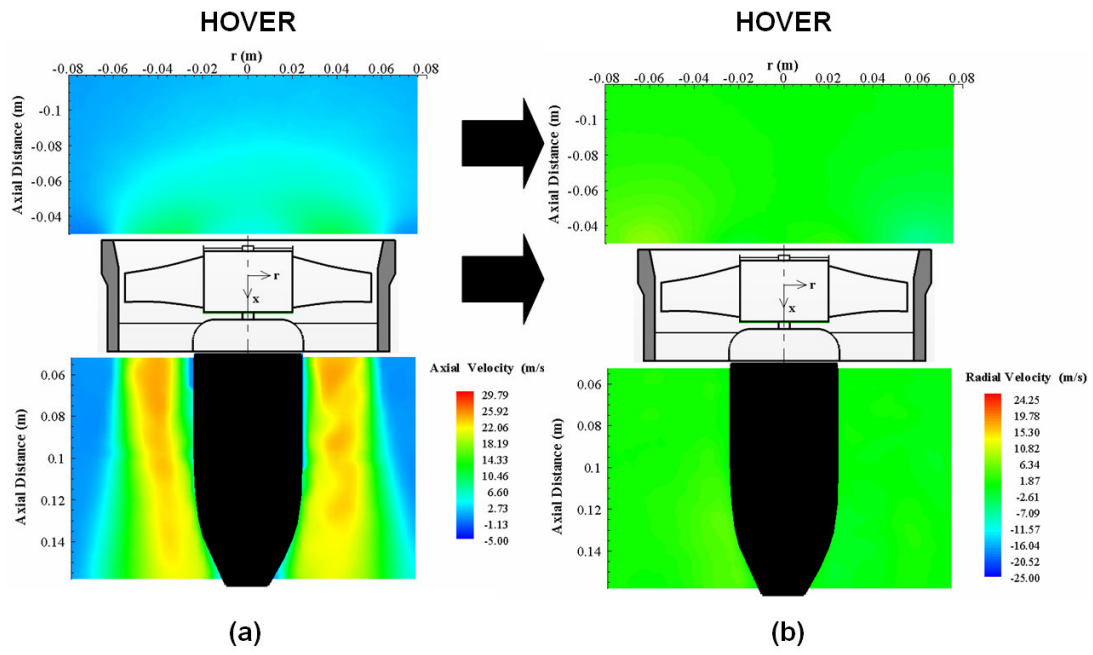


Fig. 11 Axial (a) and Radial (b) velocity components at HOVER condition (PIV measurements at 9000 rpm)

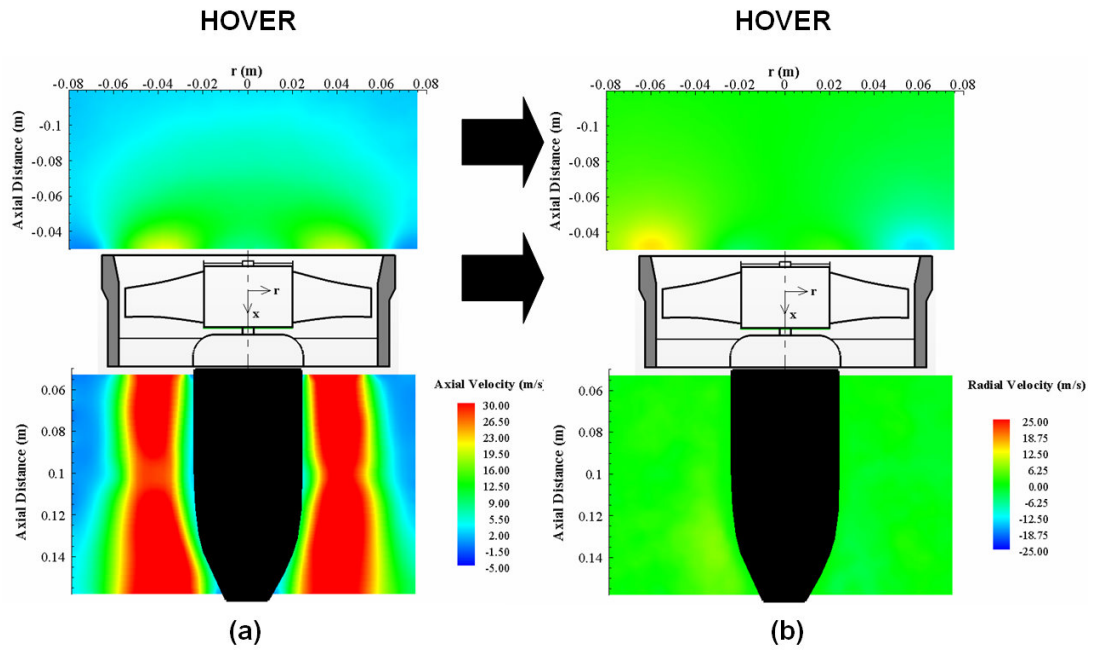


Fig. 12 Axial (a) and Radial (b) velocity components at HOVER condition (PIV measurements at 15000 rpm)

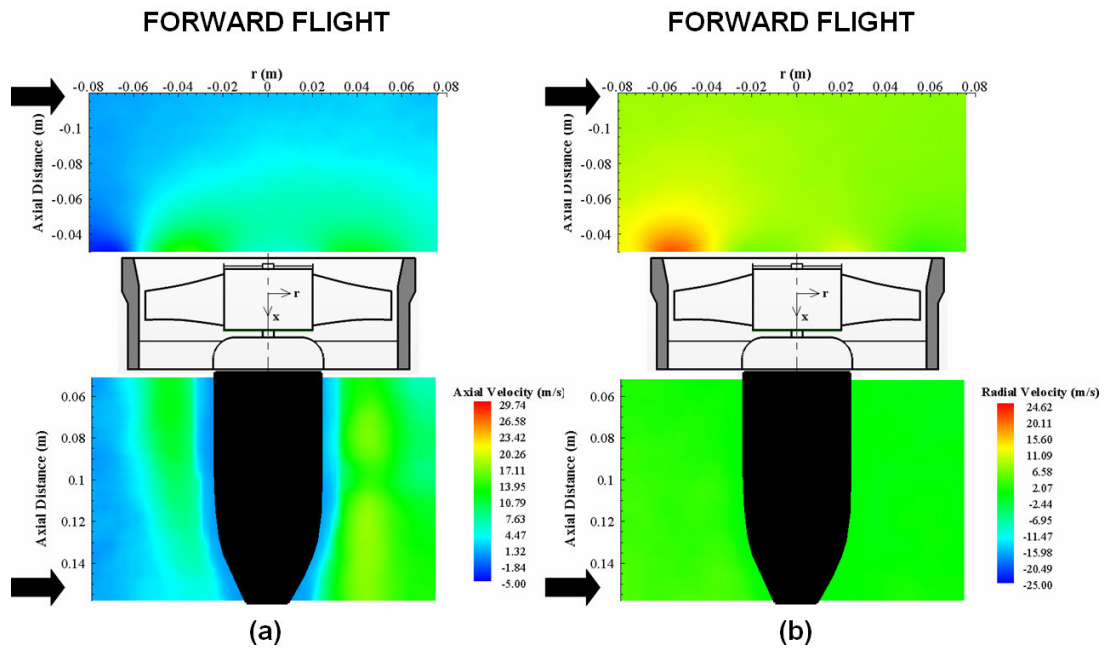


Fig. 13 Axial (a) and Radial (b) velocity components at FORWARD FLIGHT condition (PIV measurements at 9000 rpm)

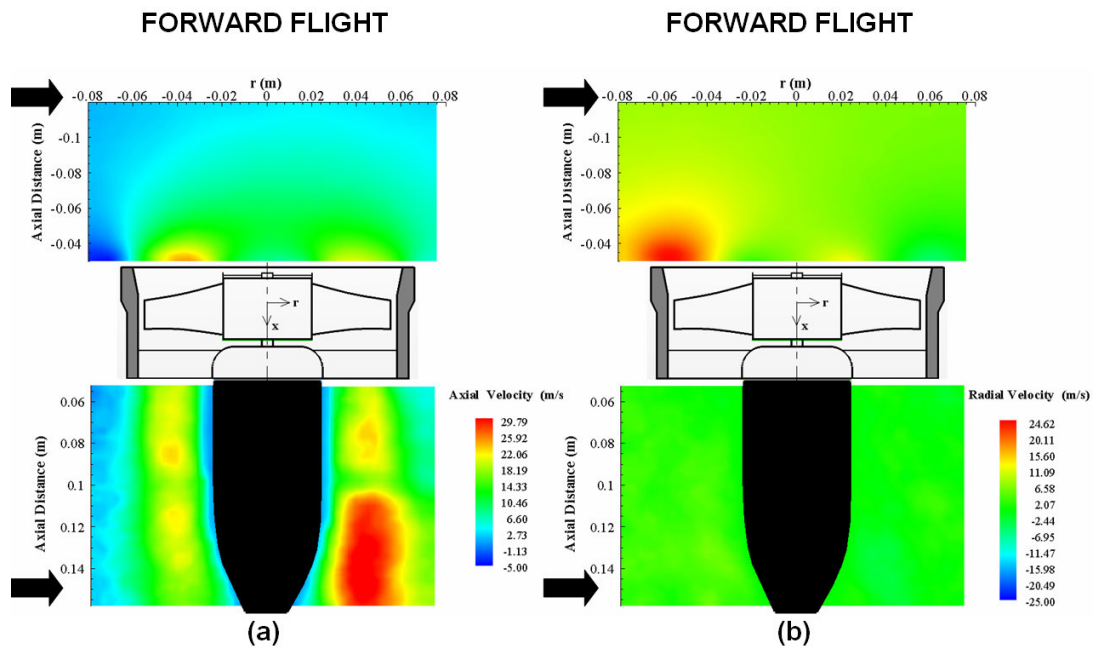


Fig. 14 Axial (a) and Radial (b) velocity components at FORWARD FLIGHT condition (PIV measurements at 15000 rpm)

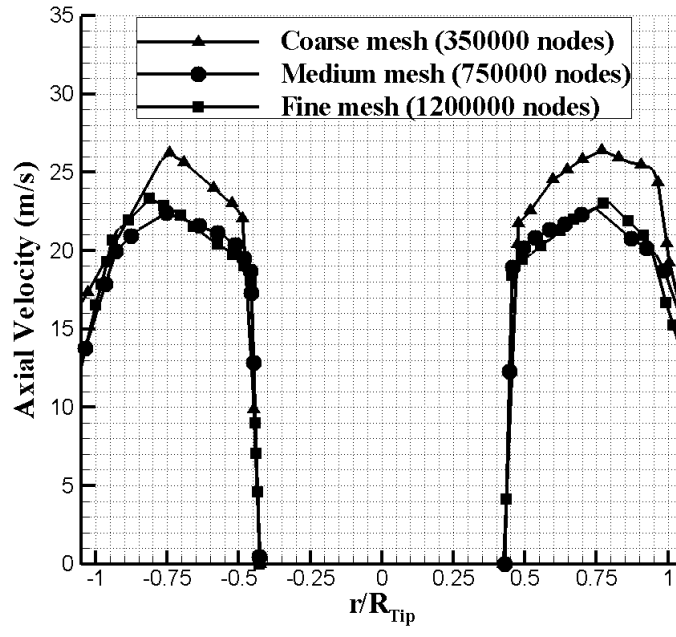
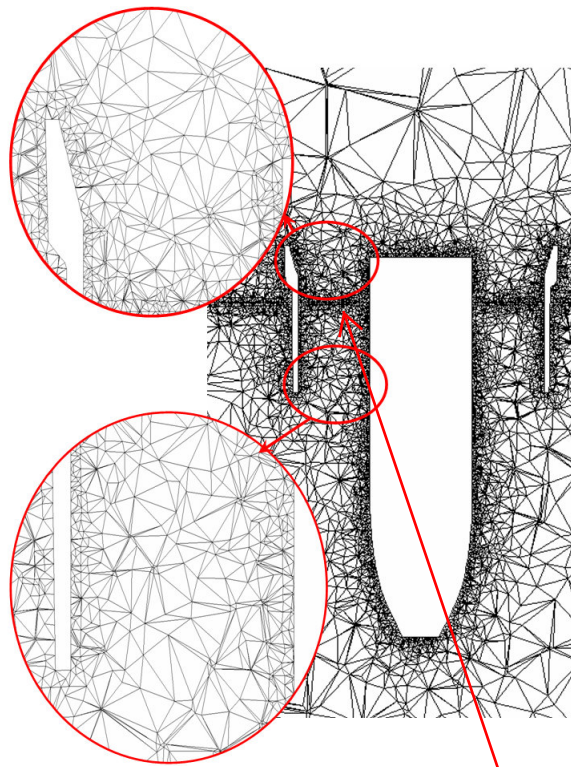


Fig. 15 Grid indepenence study



← make sure circles are circles
ellipses are ellipses
avoid unnecessary stretching

Fig. 16 Medium mesh used in computations

clearly mark the location of the rotor disk
may be a thick line and text ..

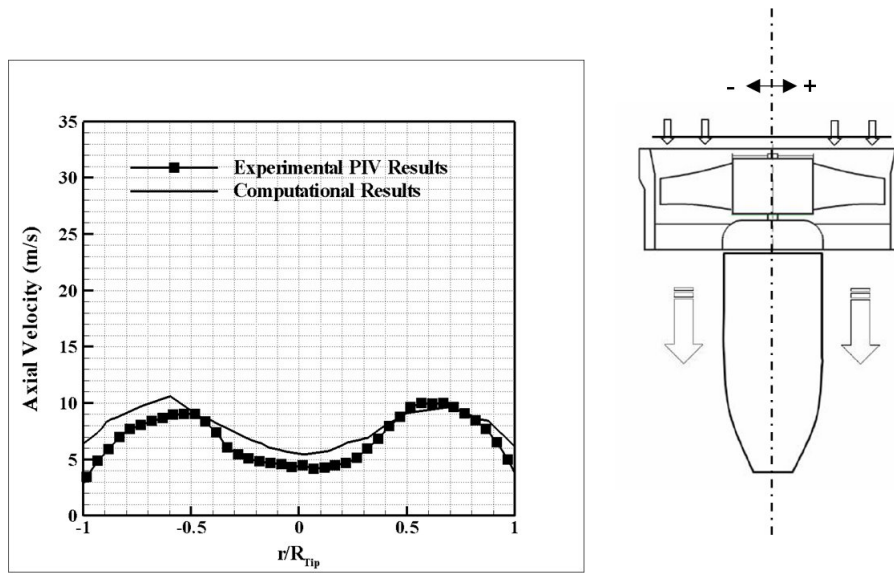


Fig. 17 Comparison of axial velocity at fan inlet 3 mm away from the duct surface at hover condition 9000 rpm.

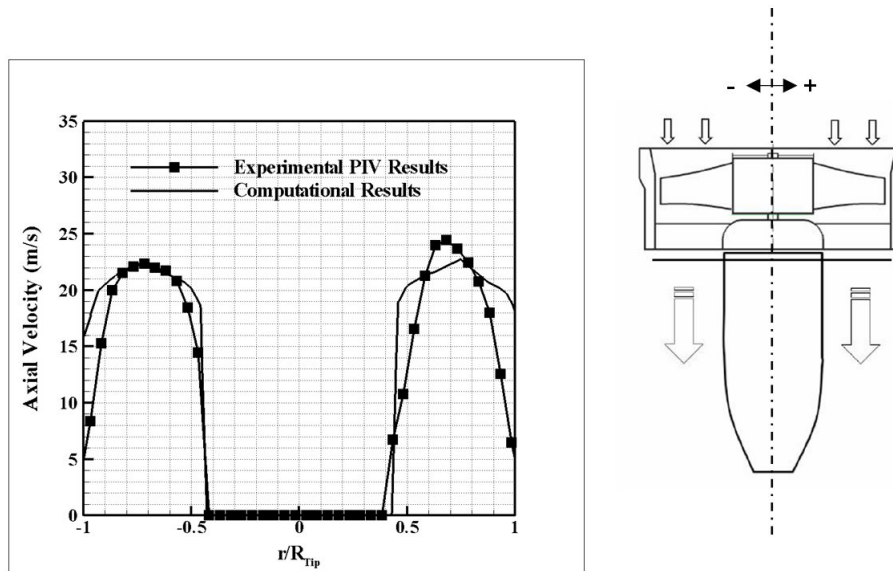


Fig. 18 Comparison of axial velocity at fan exit 3 mm away from the duct surface at hover condition 9000 rpm.

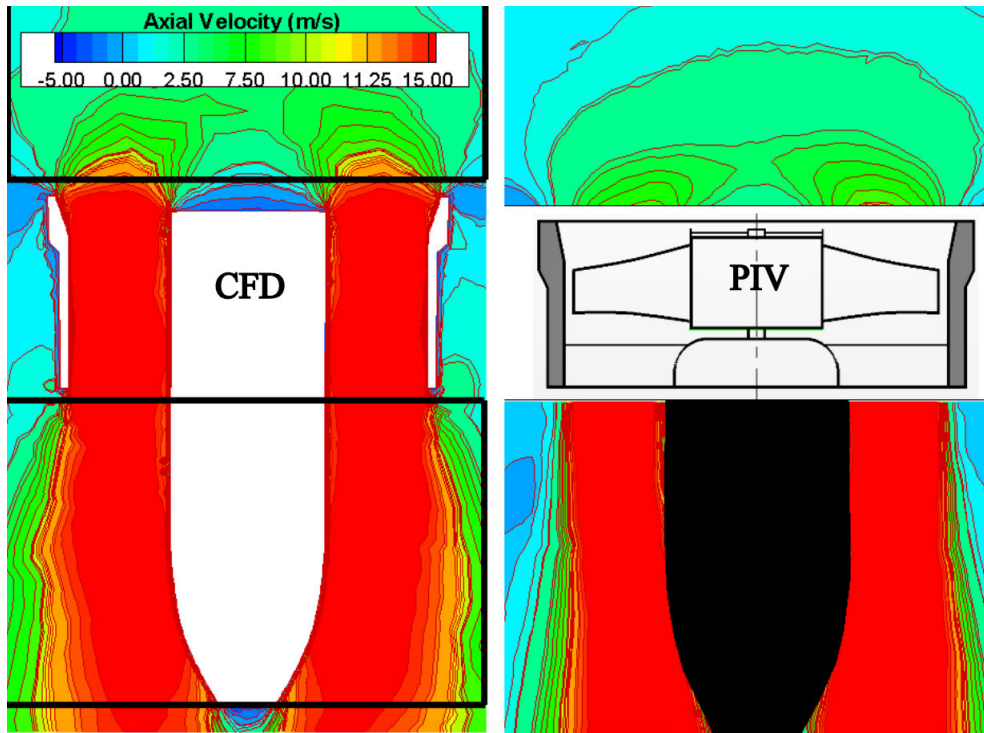


Fig. 19 Comparison of CFD and PIV axial velocity contours at hover condition at hover condition 9000 rpm.

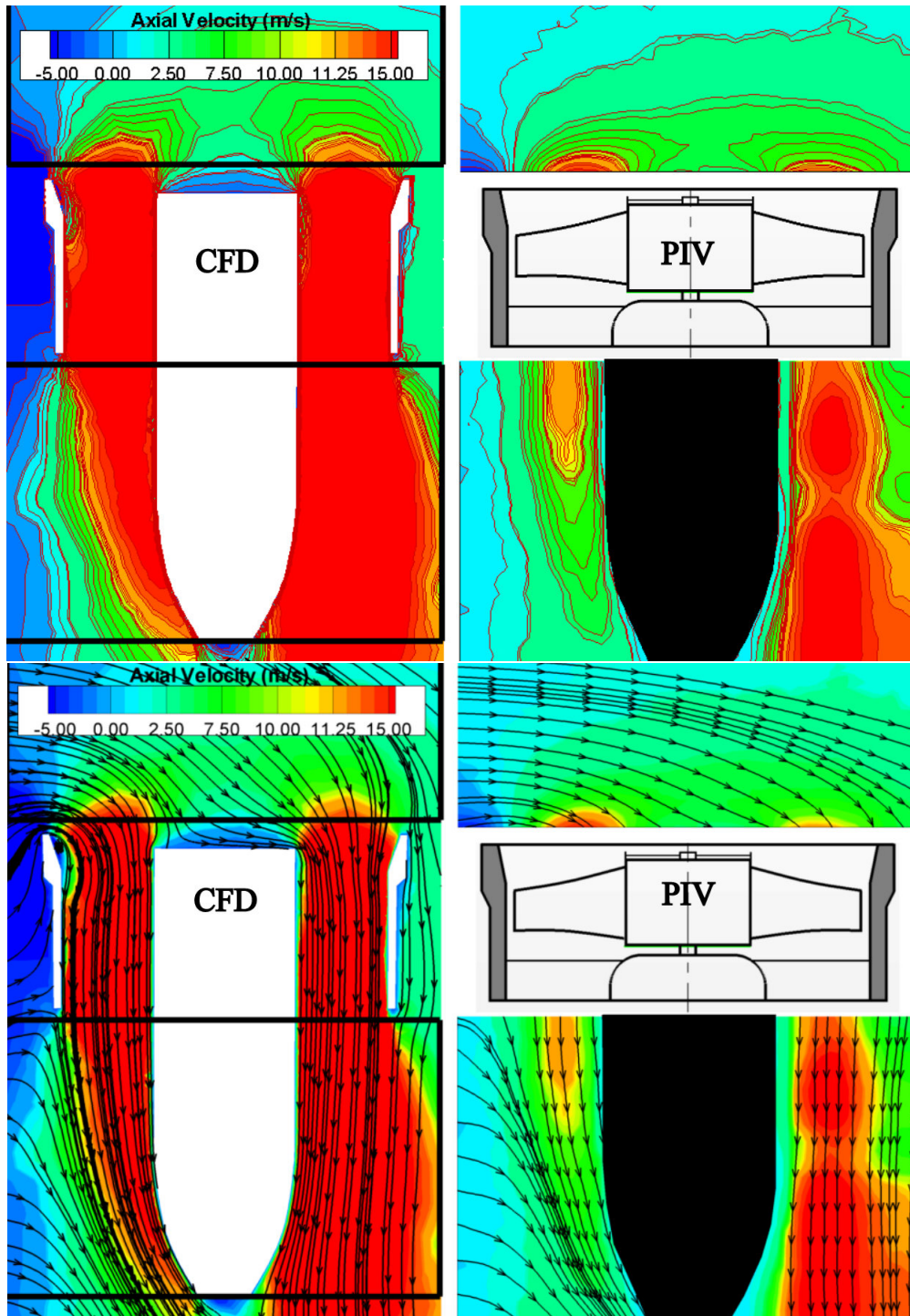


Fig. 20 Comparison of CFD and PIV axial velocity contours and streamlines at forward flight
9000 rpm and 6 m/s.

Ali

For FUTURE papers...
Please stick to the same font
you tend to mix fonts

each figure has its own style

In archival publishing we stick to the common style/fonts/line thicknesses/symbol styles